remote sensing

MDPI

Communication

Ionospheric Changes over the Western Pacific Ocean near and after the End of Annular Solar Eclipse on 21 June 2020

Jin Wang [1], Tao Yu [1,*], Yu Liang [1], Xiangxiang Yan [1,2], Chunliang Xia [1] and Yifan Qi [1]

[1] School of Geophysics and Geomatics, China University of Geosciences, Wuhan 430074, China
[2] Ministry of Education Key Laboratory of Geological Survey and Evaluation, China University of Geosciences, Wuhan 430074, China
* Correspondence: yutao@cug.edu.cn; Tel.: +86-18162307810

Abstract: The center path of the 21 June 2020 solar eclipse, which passed through Guam (13.62°N, 144.86°E, 94.6% obscuration), United States, at the end of its journey, provides a peculiar opportunity to study the ionospheric changes as the moon shadow moves into the nightside. In this study, remote-sensing observations of the ionosphere taken from the ionosonde, and total electron content from the International GNSS Service over Guam were analyzed to examine the related ionospheric changes. Independent in situ observations of electron density (N_e), electron (T_e) and ion temperatures (T_i) from DMSP-F17 at ~850 km, and N_e and T_e from Swarm-B at ~540 km were also studied. With a significant enhancement of the critical frequency and downward movement of F_2-layer, the ionosphere was compressed as the moon shadow swept over Guam near its sunset hours. Neutral wind observations from the Ionospheric Connection Explorer (ICON) showed the westward reversed wind occurring in the *F*-region near sunset. The westward wind disturbance and downward press over the Western Pacific suggest changes in the electrodynamics in the ionosphere and thermosphere near sunset at the end of the solar eclipse, which further contributes to ~85% decrease of N_e and 157% enhancement of T_e at ~540 km near midnight.

Keywords: solar eclipse; ionosonde; ionospheric compression; electron density and temperature; sunset; electrodynamics process; low latitudes

Citation: Wang, J.; Yu, T.; Liang, Y.; Yan, X.; Xia, C.; Qi, Y. Ionospheric Changes over the Western Pacific Ocean near and after the End of Annular Solar Eclipse on 21 June 2020. *Remote Sens.* **2023**, *15*, 1389. https://doi.org/10.3390/rs15051389

Academic Editor: Michael E. Gorbunov

Received: 13 January 2023
Revised: 10 February 2023
Accepted: 27 February 2023
Published: 1 March 2023

1. Introduction

Solar eclipses can cause a transient sunset and sunrise process in the Earth's atmosphere, which occurs when the moon moves directly between the Sun and the Earth. Most studies have shown that the moon shadow can not only disturb the thermosphere and ionosphere during the obscuration [1–5], but can also cause thermospheric and ionospheric perturbations near and after sunset [6–12].

Yeh et al. showed the decreased electron density near sunset at low latitudes on the day of the 24 October 1995 solar eclipse [7]. They suggested that the reduced ionospheric conductivity as well as the weakened pre-reversal enhancement (PRE) near sunset are the main cause of the electron density depression. Tsai and Liu showed that the total electron content (TEC) observed by the global positioning system (GPS) experienced sunset ascension and secondary depression before/around and after local sunset during solar eclipses on 24 October 1995 and 9 March 1997. They suggested that the enhanced PRE induced by the two solar eclipses near sunset plays an important role in this phenomenon [8]. Liu et al. studied the eclipse on 20 August 2017 and their results revealed that the lunar tide can be a factor in the ionospheric disturbance after an eclipse at night [9]. Harding et al. showed that the 21 August 2017 total solar eclipse caused the thermospheric neutral wind disturbances to behave as a large-scale thermospheric wave that propagated from the sunset terminator and emphasized the night side [12]. Aryal et al. presented the first global-scale synoptic observations of the eclipse's effect on the thermosphere during the 2 July 2019

solar eclipse and showed that the ΣO/N2 column density ratio within the totality path was enhanced during and after the eclipse [5]. Sun et al. studied the Global Navigation Satellite System (GNSS) TEC behaviors during and after the 21 June 2020 annular solar eclipse and showed that the eclipse could disturb the electrodynamics process near sunset and cause the nighttime TEC perturbations to behave as a large-scale thermospheric terminator wave propagating after sunset [10]. Wang et al. suggested that the solar eclipse-induced convergence effects disturbed the ionosphere from the obscuration to near midnight and caused long-lasting ionospheric perturbations near the center path of the moon shadow during the solar eclipse of 21 June 2020 [11].

Numerous studies, as mentioned above, have analyzed the ground-based GNSS TEC observations and showed the ionospheric disturbances after the eclipse near sunset. The TEC is an efficient and economical data set to study an ionospheric weather phenomenon, but it is an integration value. The ionosondes can observe the altitudinal profiles of the plasma density structure of the ionosphere [6,11,13], which can reveal the mechanism contributing to the ionospheric changes. However, ionosonde observations for analyzing the ionospheric changes at the end of the solar eclipse are rare [14,15]. Sridharan et al. studied the ionospheric changes over Trivandrum, India with ~69% obscuration during the 11 August 1999 total solar eclipse that occurred near sunset, and showed that the partial solar eclipse could increase the post-sunset *F*-layer [14]. Chen et al. showed that the 15 January 2010 annular solar eclipse moving into the sunset terminator at middle latitudes in Eastern China could enhance the PRE, as well as the critical frequency of the F_2-layer (f_oF_2) in the area, with ~20-82% obscuration [15]. Note that the ionospheric responses to the solar eclipses near sunset, as shown in all the studies, either have a time difference between the last contact of the moon shadow over the locations of the ionospheric instruments and the local sunset [7–11], or are beyond the center path of the moon shadow [14,15].

Fortunately, an annular solar eclipse occurring on 21 June 2020 ended over Guam, (13.62°N, 144.86°E) in the Western Pacific Ocean, with 94.8% obscuration (near the center path) near its local sunset hours. The remote-sensing observations of the ionosphere based on the local ground observations from ionosonde and GNSS TEC exist there, which is rare and provides a precious opportunity to investigate the ionospheric changes near the center path of the solar eclipse as the moon shadow meets the sunset terminator over the Western Pacific Ocean. Moreover, the in situ satellite observations from Defense Meteorological Satellite Program (DMSP) F17 spacecraft and Swarm-B satellite pass nearby, which allows us to show a comparison with the remote sensing results. The neutral wind data derived from the remote observations of red 630.0 nm airglow emissions from the Michelson Interferometer for Global High-resolution Thermospheric Imaging (MIGHTI) instrument onboard the Ionospheric Connection Explorer (ICON) satellite [16] were also analyzed to explore the corresponding mechanism.

Figure 1 shows the geomagnetic and solar activity on the day of the 21 June solar eclipse and the three days before. The geomagnetic condition was stable with Kp $\leq$ 1+ and Auroral Electrojet (AE) index $\leq$ 280 nT, and the solar activity was quiet with F10.7 = 69.9 s.f.u on the eclipse day. The day before the solar eclipse day was disturbed by a substorm (Figure 1b); therefore, the days 18–19 June 2020 were chosen as the reference days.

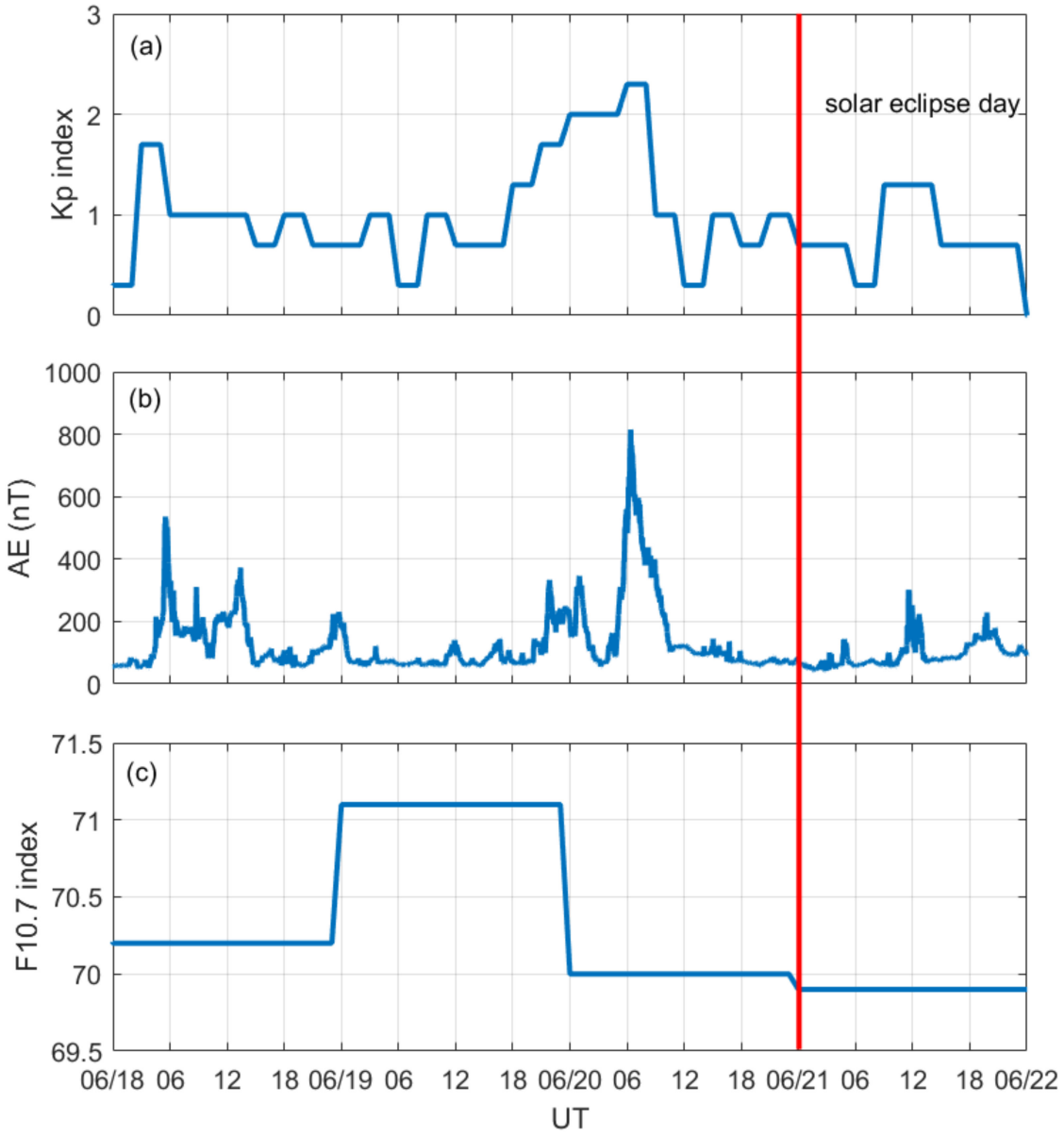

Figure 1. Geomagnetic and solar condition on the 21 June 2020 solar eclipse and three days before. (**a**) Kp, (**b**) Auroral Electrojet (AE) and (**c**) F10.7 index.

2. Data

Figure 2 illustrates the location of the ionosonde, and the ground track of the DMSP F17 spacecraft and Swarm-B satellite on the solar eclipse day and the reference days. The ionogram data recorded by Guam ionosonde (13.62°N, 144.86°E) were manually scaled to obtain f_oF_2, the peak height of the F_2-layer (h_mF_2), and the plasma density profiles, by employing the SAO Explorer [17]. The TEC data over Guam was derived from the binary file [10], which is available at the International GNSS Service (IGS). The data with elevation angle $\geq 40°$ were analyzed here to avoid the possible tropospheric and multipath effects. The DMSP F17 spacecraft passed through the moon penumbra near the local sunset over Guam and recorded the ionospheric electron density (N_e), electron temperature (T_e), and ion temperature (T_i) behaviors at ~850 km. The Swarm-B satellite orbits the earth at ~540 km and can record the N_e and T_e.

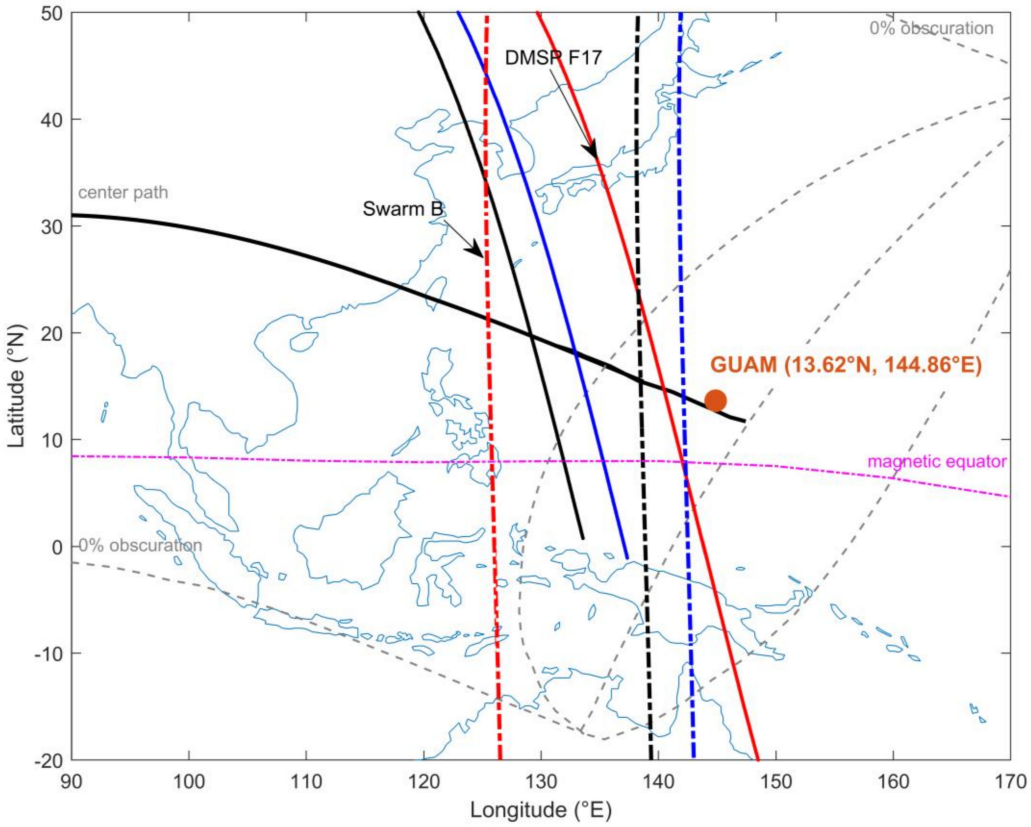

Figure 2. Locations of the ionosonde (brown circle), the ground-track of Swarm-B satellite (dotted lines), and DMSP F17 spacecraft (solid lines) paths. The red indicates the satellite tracks on the solar eclipse day (21 June 2020). The black and blue indicate the satellite tracks on 18 and 19 June 2020, respectively. The magenta line represents the magnetic equator. The gray and black curves indicate the eclipse path. The GNSS receiver at Guam used in this study is not displayed in Figure 2, because it is near the location of ionosonde.

3. Results

Figure 3 shows a height-time-amplitude (HTA) plot of the echoes recorded by the Guam ionosonde on the 21 June 2020 solar eclipse and compares the f_oF_2 and h_mF_2 behaviors on the solar eclipse day and the reference days. The HTA is the integration of the echo amplitude over the sounding frequencies from 1.0 to 15.0 MHz at each altitude [10]. The echoes exhibit an obvious downward movement after the local sunset at sea level (08:50 UT, 18:30 LT, LT = UT + 9.66) over Guam, and reach their minimum height at ~200 km near 11:00 UT (20:40 LT). During the downward movement process, the f_oF_2 increases from 6.1 to 11.63 MHz (Figure 3b) and the h_mF_2 moves downward from 312.5 to 204.1 km (Figure 3c) at 09:00–10:45 UT (18:40–20:25 LT). The downward velocity is ~17.2 m/s (the h_mF_2 deviation/time interval). Note that the f_oF_2 weakens during the solar eclipse period, which is expected due to the moon obscuration.

Figure 4 shows the evolution of the plasma density profiles derived from the Guam ionogram using the SAO explorer software 3.6.1 and compares the TEC behaviors near Guam on the solar eclipse day and the reference days. With a decreased plasma density at higher altitudes and increased plasma density at lower altitudes (Figure 4a), the plasma density profile over Guam narrows gradually during the period of 09:15–10:45 UT. The decrease in TEC since the beginning of the solar eclipse is expected due to the obscuration of moon shadow on the solar eclipse day (Figure 4b). However, the TEC stops its decreasing trend near 09:30 UT (~19:10 LT), maintains the values till ~10:50 UT (~20:30 LT), and decreases quickly after then. This tendency differs from the typical TEC behaviors that decline all the way after ~09:00 UT (~18:40 LT, near sunset) on the reference days. The

maintaining of the TEC value occurs during the period of the ionospheric downward process (Figure 4a) on the solar eclipse day. Note that the TEC on the solar eclipse day remains extremely low after ~11:20 UT (~21:00 LT) in the nighttime.

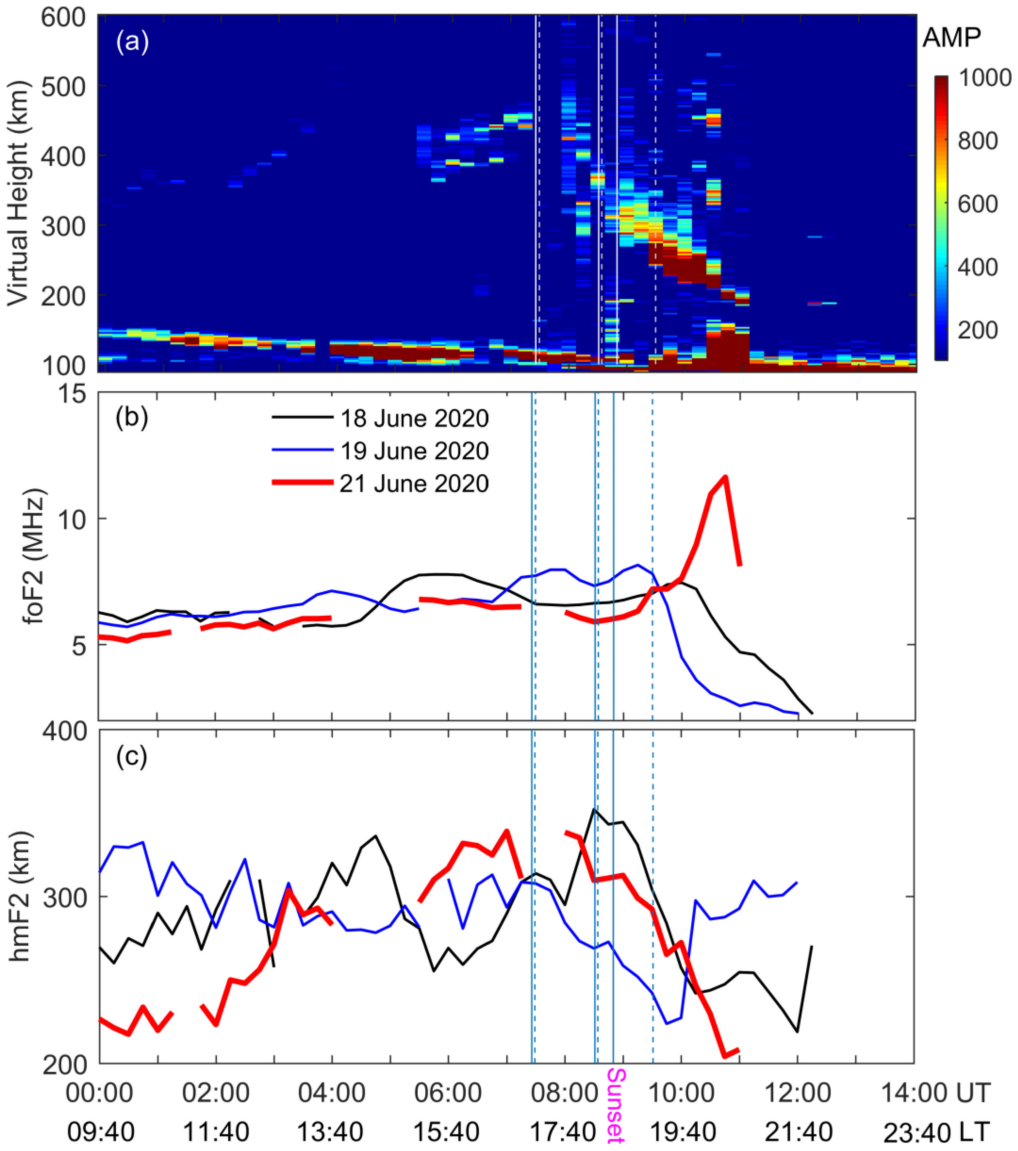

Figure 3. Evolution of the height-time-amplitude (HTA) and the critical frequency (f_oF_2) and peak height (h_mF_2) of the F_2 layer on the solar eclipse day (red line) and the reference days (18–19 June). (**a**) The HTA plot on the solar eclipse day. (**b**) The f_oF_2 and (**c**) h_mF_2 plot on the solar eclipse day (red) and reference days. The solid vertical lines represent the beginning, maximum obscuration of the solar eclipse, and the sunset time at sea level (~0 km). The dotted vertical lines represent the beginning, maximum, and end of the obscuration at ionospheric height (~200 km).

Figure 5 shows the DMSP F17-observed N_e, T_e, and T_i behaviors at ~850 km to show the ionospheric changes at high altitudes near sunset over Guam. Figure 5a shows that notable N_e decrease occurs at high altitude near sunset on the solar eclipse day. The N_e over the latitude of Guam weakens by ~20% (reduced from ~2.5 × 10^{10} to ~2.0 × 10^{10}) compared with the reference days. The decreased N_e phenomenon covers a much wider latitudinal belt (~20°S–46°N geomagnetic latitude), which agrees with the TEC decease near the western coast of Pacific during the obscuration [10,18]. The T_e and T_i also exhibit obvious perturbations on the solar eclipse day (Figure 5b–c). The T_e enhances at ~10–50°N geomagnetic latitudes, while it slightly decreases near the magnetic equator (Figure 5b).

The T_i is much enhanced within 0–17.1°N geomagnetic latitudes (Figure 5c). The maximum increase of T_i is up to ~565 K (from 1310 K to 1875 K) near 10°N geomagnetic latitude.

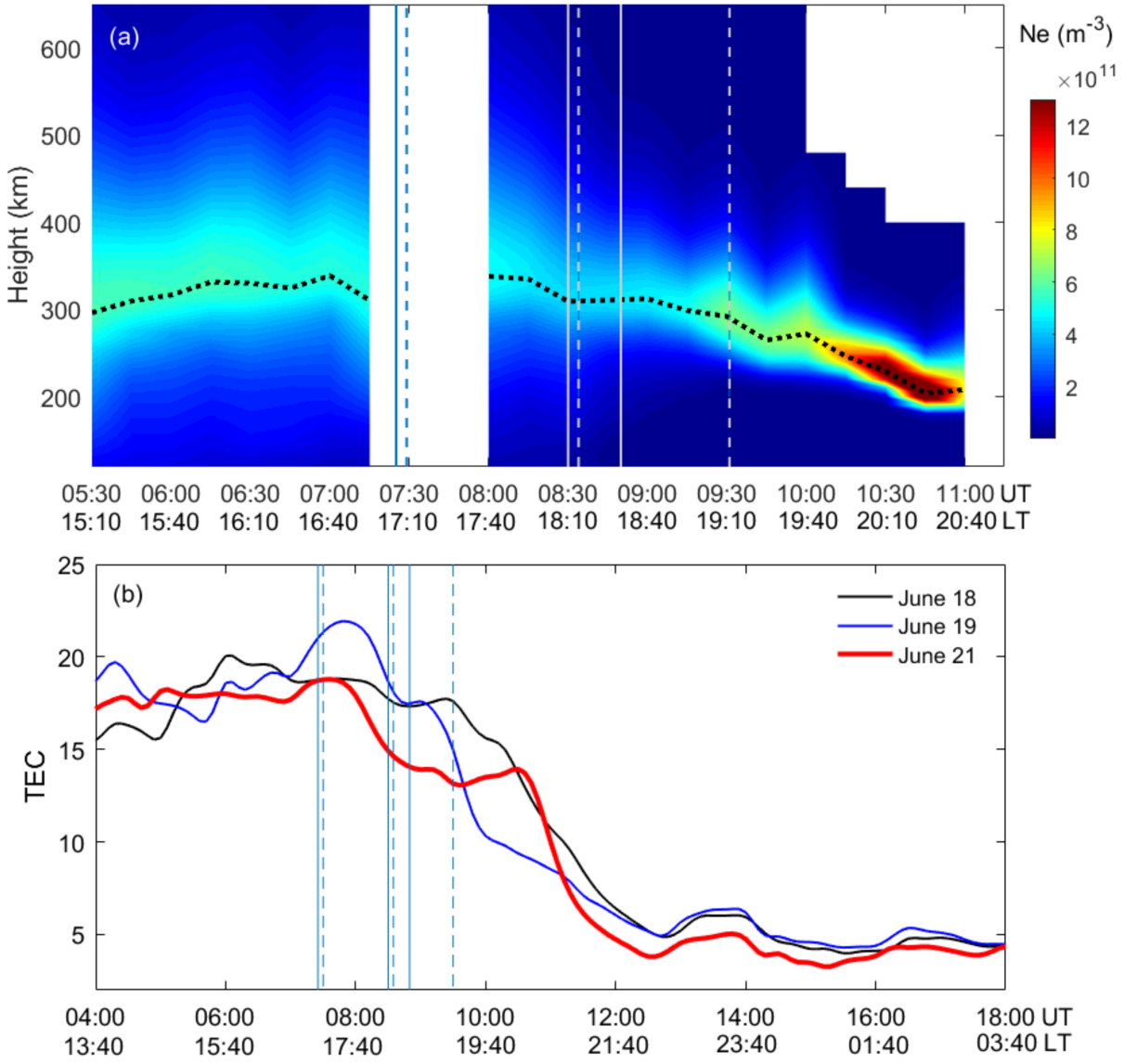

Figure 4. The plasma density profiles and total electron density content (TEC) recorded over Guam. (**a**) The plasma density profile derived from the ionogram recorded by Guam ionosonde on the solar eclipse day. The black dotted line represents the evolution of *h*mF2. (**b**) The comparison of TEC on the solar eclipse day (red line) and the reference days.

Since the TEC remains extremely low after 21:00 LT (Figure 4b), the changes in N_e and T_e observed by Swarm-B (Figure 6) at ~540 km near midnight were examined to further investigate the nighttime ionospheric behaviors at high altitude. The N_e and T_e near midnight also show significant perturbations, which mainly occur near the magnetic equator on the solar eclipse day. The N_e largely decreases within ~12.4°S–7.8°N latitude (Figure 6a), while the T_e shows a remarkable enhancement (up to ~2000 K) within the same latitudes (Figure 6b). Compared with the reference days, the N_e decreases by ~85% (from ~3.753×10^4 to ~0.53×10^4) and the T_e increases by 157% (from ~1626 K to ~4186 K) near the magnetic equator. The behaviors of N_e and T_e show an obvious anti-correlation.

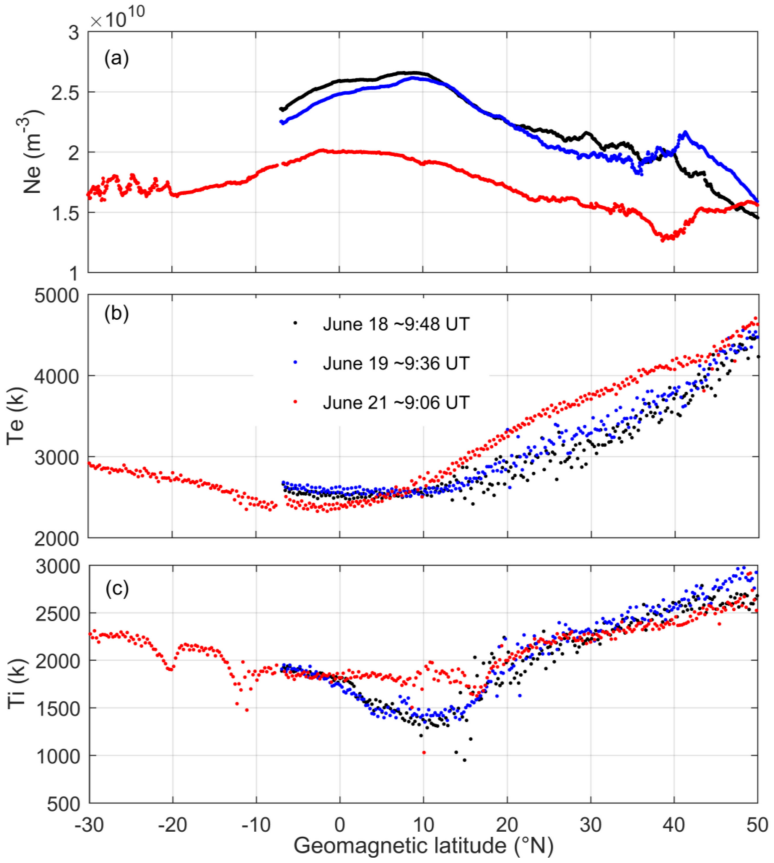

Figure 5. DMSP F17-observed (**a**) electron density (N_e), (**b**) electron temperature (T_e) and (**c**) ion temperature (T_i) behaviors near local sunset (~18:30 LT) on the solar eclipse day and reference days.

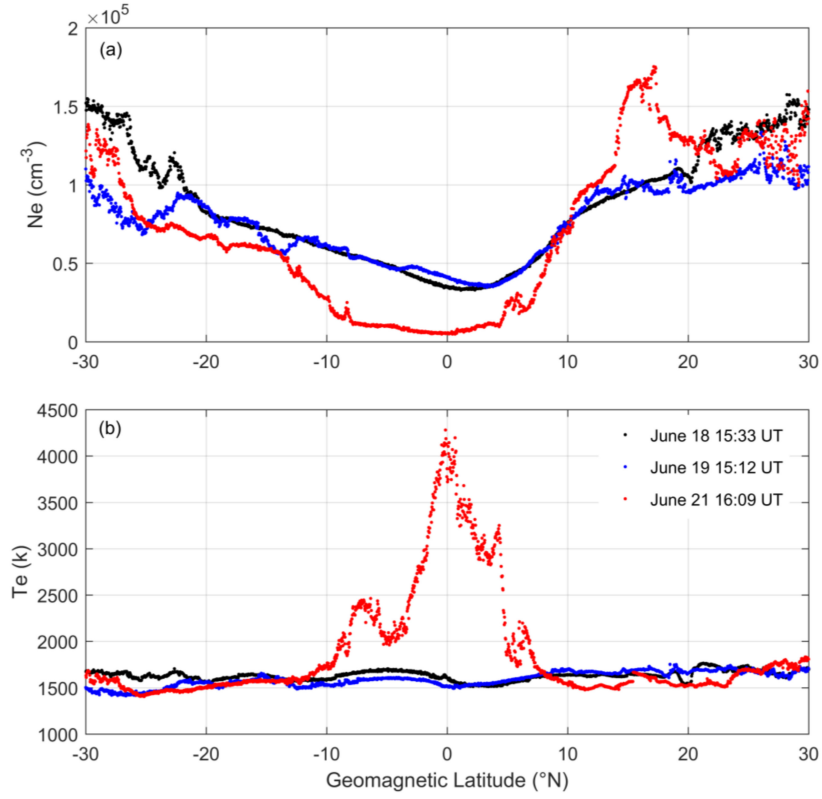

Figure 6. Swarm-B observed (**a**) N_e and (**b**) T_e in the nighttime on the solar eclipse day and reference days.

4. Discussion

The enhanced f_oF2 behavior over Guam (Figure 3b) as the moon shadow moves into the sunset terminator on the solar eclipse of 21 June 2020 agrees with the observations of Chen et al. [15]. However, the mechanism responsible for the enhancement should be different between the different eclipse events. Chen et al. suggested that the enhanced PRE with a rapid upward movement of the F_2-layer near sunset and the following westward electric field contributed to the enhanced f_oF_2 at mid-latitudes near sunset during the 15 January 2010 annular solar eclipse period [13]. The upward movement of the post-sunset *F*-layer over Trivandrum, India following the 11 August 1999 solar eclipse was also observed by Sridharan et al. [14]. However, in this study, the ionosonde of Guam shows no upward movement of the *F*-layer and the f_oF_2 increases with a significant downward movement of h_mF_2 as the moon shadow moves into the night side at low latitudes. The results suggest that the enhanced f_oF_2 has little relationship with the PRE during this solar eclipse. In addition, the stable geomagnetic and solar condition on the solar eclipse day (Figure 1) would also have little contribution to the phenomena near sunset [10,19].

It is known that the ionospheric behavior near sunset at low latitudes is mainly dominated by the electrodynamics process, and the winds and conductivity are the main factors [20,21]. The PRE driven by the electrodynamics process should be weak at the summer solstice under solar minimum [22–24]. When the moon shadow moves toward and approaches the sunset terminator, the shadow can spread over the curved surface quickly due to the occultation geometry of the obscuration [25], and cools the ionosphere in the end of a solar eclipse. The earlier cooling of the ionosphere caused the local sunset to happen earlier over Guam, which would keep the temperature low and suppress the zonal gradients as well as the conductivity gradients that exist near the sunset terminator. Moreover, the temperature gradients near the edge of the shadow can cause disturbances in neutral wind near sunset.

The evidence for the disturbances in zonal wind was clearly recorded by the ICON-MIGHTI instrument (Figure 7). Contrary to the typically eastward-blowing wind near sunset on the reference days, a westward reversed wind occurred in the *F*-layer (160–240 km) near sunset (~18:05 LT) on the solar eclipse day. The onset of the westward disturbed wind (Figure 7b) near sunset reveals the reverse of the convection vortex that leads to the disappearing of PRE, and even contributes to the downward press (Figure 3a). These results suggest that the ionospheric wind dynamo was changed [20,26,27].

On the other hand, the eclipse geometry is different at various ionospheric heights [28]. The early cooling of the *E*-region and lower altitudes due to the approach of the moon shadow may cause an contraction effect in the vertical direction (white arrow in Figure 8), which can lead to a westward electric field due to $E = -U \times B$ (yellow arrow). The U and B represent the thermospheric winds and the magnetic field, respectively. The ionospheric contraction and westward electric field then cause the convergence of the plasma flux near the end of the obscuration (brown arrow), which results in the ionospheric compression as the density increases at low altitudes and the density decreases at high altitudes (Figure 4a).

The results are similar to the observations of Liu et al. [29,30] during the non-eclipse period. They suggested that the occurrence of plasma flux convergence could cause f_oF_2 to increase with a downward movement of the F_2-layer at low latitudes (Sanya (18.3°N, 109.6°E) and Qujing (25.6°N, 103.8°E)) near sunset during a geomagnetically quiet period. The exact reason for the convergence is unknown. In this study, the compression (Figures 3 and 4) caused by a westward wind disturbance and eclipse-induced contraction gave the ionosphere a downward press near sunset, which may originate a large-scale wave following the terminator [10].

Typically, the electron temperature yields the anti-correlation with the electron density in the topside ionosphere [31–34]. The decreased N_e at ~850 km (Figure 5a) shows an anti-correlation with the enhanced T_e (Figure 5b) within ~10-45°N geomagnetic latitude due to the weakened cooling through the collision with ions [33]. However, both T_e and N_e are reduced near the magnetic equator, which may result from the moon shadow, with 70.8%

obscuration at ~850 km there. On the other hand, the enhanced T_i (Figure 5c) near Guam may relate to the ionospheric compression due to the convergence effect, which brings hot plasma to lower altitudes and latitudes from higher places and causes the enhanced T_i around the equator [35].

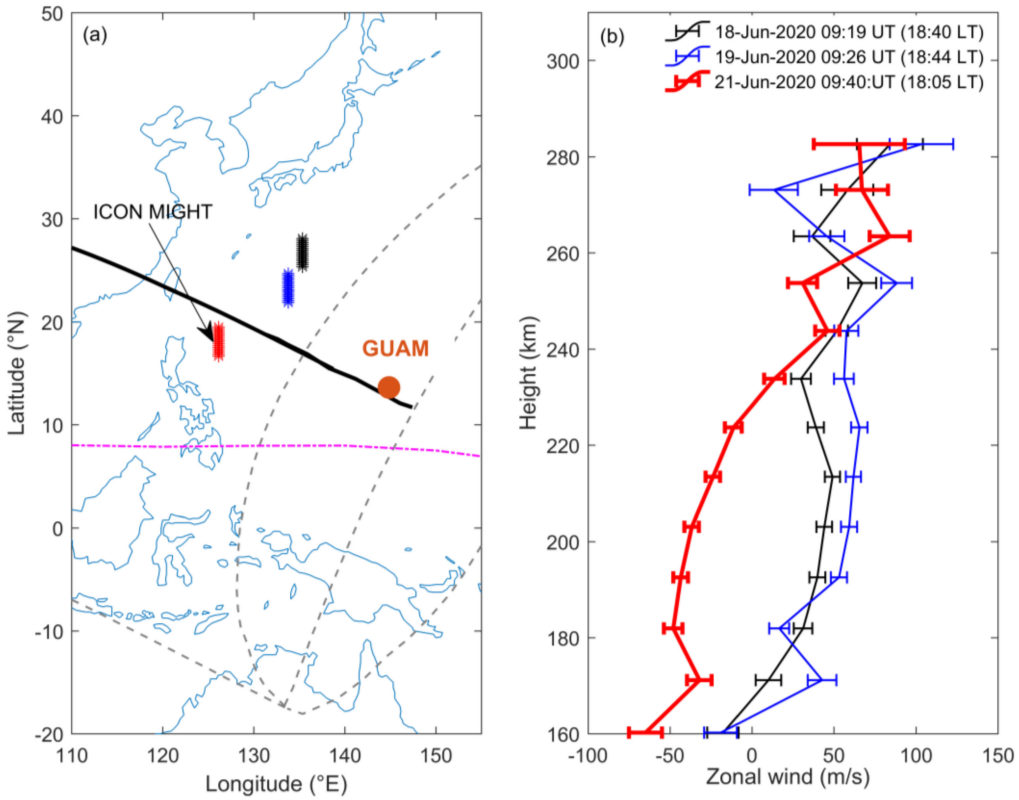

Figure 7. Zonal wind profiles observed by ICON-MIGHTI on the solar eclipse day (red) and reference days. (**a**) Locations of the ICON-MIGHTI wind. (**b**) Zonal wind profiles.

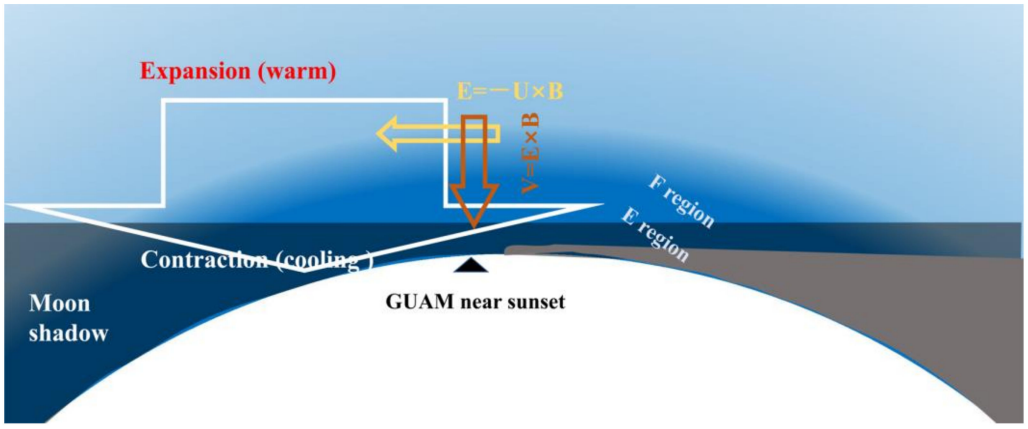

Figure 8. Illustration of the possible mechanism that contributes to the related ionospheric changes as the moon shadow meets the sunset terminator. The white arrow indicates the convergence that contains the downward press over Guam and westward wind disturbance over the western Pacific.

The prominent N_e depletion agrees with the extremely low TEC after 21:00 LT (Figure 4b), which yields an anti-correlation with the remarkable T_e enhancement. The downward press of the ionosphere (Figures 3c and 4a) brings the plasma to lower altitude where the losing rate is high, which caused the long-lasting depression. The extreme T_e enhancement near

the magnetic equator and near midnight may result from the decreased heat conduction along the magnetic field lines from the equatorial topside ionosphere with the prominent N_e depletion [33] and the ionospheric compression [35,36], which should be further investigated for future eclipse events.

5. Conclusions

This study takes advantage of the ground-based ionosonde and GNSS-TEC observations over Guam (13.62°N, 144.86°E, 94.6% obscuration), which was well located at the end of the annular solar eclipse to examine what happened as the moon shadow met the sunset on 21 June 2020. The f_oF_2 increased significantly along with an obvious downward movement of h_mF_2, while the TEC remained nearly unchanged near the local sunset hours. The independent space-based observations from DMSP-F17 near sunset also recorded the disturbed ionosphere at high altitude (~850 km) with the decreased electron density (N_e) and enhanced ion temperature there nearly during the same period. The westward wind in the *F*-layer near sunset observed by ICON-MIGHTI reveals that the convection vortex was reversed and the electrodynamics process was changed as the moon shadow coincided with the sunset. The changed electrodynamics caused the downward press of the ionosphere, which led to the enhancement of peak density but reduced the ionospheric layer height near the sunset. The reduced ionospheric layer height as well as the early sunset further led to the long-lasting extremely low density over the entire night, and then contributed to the remarkable N_e and T_e perturbations observed by Swarm-B at ~540 km near midnight. The results suggest that the occultation geometry of the moon shadow near sunset can play a significant role in the electrodynamics process at low latitudes, which should be considered in the ionospheric response to the solar eclipse in future studies.

Author Contributions: Conceptualization, J.W. and T.Y.; methodology, J.W.; software, J.W. and Y.L.; validation, T.Y., Y.L. and X.Y.; formal analysis, J.W.; investigation, J.W. and Y.Q.; resources, J.W. C.X. and T.Y.; data curation, J.W. and C.X.; writing—original draft preparation, J.W.; writing—review and editing, J.W., T.Y. and Y.L; visualization, J.W.; supervision, T.Y.; project administration, J.W. and T.Y.; funding acquisition, J.W. and T.Y. All authors have read and agreed to the published version of the manuscript.

Funding: This research was funded by National Natural Science Foundation of China, grant number 42104165; 42230207, and the Fundamental Research Funds for the Central Universities, China University of Geosciences (Wuhan).

Data Availability Statement: The ionosonde data are available at ftp://ftp.ngdc.noaa.gov/ionosonde, accessed on 20 October 2022. The GNSS-TEC product is available at the link https://stdb2.isee.nagoya-u.ac.jp/GPS/shinbori/AGRID2/nc/index.html, accessed on 3 February 2023. The Swarm-B data can be downloaded from http://earth.esa.int/swarm/, accessed on 20 October 2022. The DMSP F17 Data are available at https://satdat.ngdc.noaa.gov/dmsp/data/, accessed on 20 October 2022. The AE index can be downloaded from https://supermag.jhuapl.edu/, accessed on 4 February 2023. The Kp and F10.7 index can be downloaded from https://omniweb.gsfc.nasa.gov/ow.html, accessed on 4 February 2023. The ICON data can be retrieved from the ICON website https://icon.ssl.berkeley.edu/Data, accessed on 28 December 2022.

Acknowledgments: The authors acknowledge the uses of the ionospheric data from the USAF NEXION Digisonde network. We appreciate International GNSS Service (IGS) for providing the GNSS-TEC data. We also appreciate the ICON and Swarm engineering and science teams for providing the ICON-MIGHTI and Swarm data. .

Conflicts of Interest: The authors declare no conflict of interest.

References

1. Rishbeth, H. Eclipse effects in the ionosphere. *Nature* **1970**, *226*, 1099–1100. [CrossRef] [PubMed]
2. Liu, J.Y.; Sun, Y.Y.; Kakinami, Y.; Chen, C.H.; Lin, C.H.; Tsai, H.F. Bow and stern waves triggered by the Moon's shadow boat. *Geophys. Res. Lett.* **2011**, *38*, L17109. [CrossRef]

3. Dang, T.; Lei, J.H.; Wang, W.B.; Yan, M.D.; Ren, D.X.; Huang, F.Q. Prediction of the thermospheric and ionospheric responses to the 21 June 2020 annular solar eclipse. *Earth Planet. Phys.* **2020**, *4*, 231–237. [CrossRef]
4. Zhang, R.; Le, H.; Li, W.; Ma, H.; Yang, Y.; Huang, H.; Li, Q.; Zhao, X.; Xie, H.; Sun, W.; et al. Multiple technique observations of the ionospheric responses to the 21 June 2020 solar eclipse. *J. Geophys. Res. Space Phys.* **2020**, *125*, e2020JA028450. [CrossRef]
5. Aryal, S.; Evans, J.S.; Correira, J.; Burns, A.G.; Wang, W.; Solomon, S.C.; Laskar, F.I.; McClintock, W.E.; Eastes, R.W.; Dang, T.; et al. First global-scale synoptic imaging of solar eclipse effects in the thermosphere. *J. Geophys. Res. Space Phys.* **2020**, *125*, e2020JA027789. [CrossRef] [PubMed]
6. Chen, G.; Wu, C.; Huang, X.; Zhao, Z.; Zhong, D.; Qi, H.; Huang, L.; Qiao, L.; Wang, J. Plasma flux and gravity waves in the midlatitude ionosphere during the solar eclipse of 20 May 2012. *J. Geophys. Res. Space Phys.* **2015**, *120*, 3009–3020. [CrossRef]
7. Yeh, K.C.; Yu, D.C.; Lin, K.H.; Huang, C.R.; Tsai, W.H.; Liu, J.Y.; Xu, J.S.; Igarashi, K.; Xu, C.; Nam, V.H. Ionospheric response to a solar eclipse in the equatorial anomaly region. *Terr. Atmos. Ocean. Sci.* **1997**, *8*, 165–178. [CrossRef]
8. Tsai, H.F.; Liu, J.Y. Ionospheric total electron content response to solar eclipses. *J. Geophys. Res.* **1999**, *104*, 12657–12668. [CrossRef]
9. Liu, J.Y.; Wu, T.-Y.; Sun, Y.-Y.; Pedatella, N.M.; Lin, C.-Y.; Chang, L.C.; Chiu, Y.C.; Lin, C.H.; Chen, C.H.; Chang, F.Y.; et al. Lunar tide effects on ionospheric solar eclipse signatures: The August 21, 2017 event as an example. *J. Geophys. Res. Space Phys.* **2020**, *125*, e2020JA028472. [CrossRef]
10. Sun, Y.-Y.; Chen, C.-H.; Qing, H.; Xu, R.; Su, X.; Jiang, C.; Yu, T.; Wang, J.; Hairu, X.; Lin, K. Nighttime ionosphere perturbed by the annular solar eclipse on June 21, 2020. *J. Geophys. Res. Space Phys.* **2021**, *126*, e2021JA029419. [CrossRef]
11. Wang, J.; Sun, Y.-Y.; Yu, T.; Wang, Y.; Mao, T.; Yang, H.; Xia, C.; Yan, X.; Yang, N.; Huang, G.; et al. Convergence effects on the ionosphere during and after the annular solar eclipse on 21 June 2020. *J. Geophys. Res. Space Phys.* **2022**, *127*, e2022JA030471. [CrossRef]
12. Harding, B.J.; Drob, D.P.; Buriti, R.A.; Makela, J.J. Nightside detection of a large-scale thermospheric wave generated by a solar eclipse. *Geophys. Res. Lett.* **2018**, *45*, 3366–3373. [CrossRef]
13. Wang, J.; Zuo, X.; Sun, Y.-Y.; Yu, T.; Wang, Y.; Qiu, L.; Mao, T.; Yan, X.; Yang, N.; Qi, Y.; et al. Multilayered sporadic-E response to the annular solar eclipse on June 21, 2020. *Space Weather* **2021**, *19*, e2020SW002643. [CrossRef]
14. Sridharan, R.; Devasia, C.V.; Jyoti, N.; Tiwari, D.; Viswanathan, K.S.; Subbarao, K.S.V. Effects of solar eclipse on the electrodynamical processes of the equatorial ionosphere: A case study during 11 August 1999 dusk time total solar eclipse over India. *Ann. Geophys.* **2002**, *20*, 1977–1985. [CrossRef]
15. Chen, G.; Zhao, Z.; Ning, B.; Deng, Z.; Yang, G.; Zhou, C.; Yao, M.; Li, S.; Li, N. Latitudinal dependence of the ionospheric response to solar eclipse of 15 January 2010. *J. Geophys. Res.* **2011**, *116*, A06301. [CrossRef]
16. Immel, T.J.; England, S.L.; Mende, S.B.; Heelis, R.A.; Englert, C.R.; Edelstein, J.; Frey, H.U.; Korpela, E.J.; Taylor, E.R.; Craig, W.W. The ionospheric connection explorer mission: Mission goals and design. *Space Sci. Rev.* **2018**, *214*, 13. [CrossRef]
17. Huang, X.; Reinisch, B.W. Vertical electron profiles from the digisonde network. *Adv. Space Res.* **1996**, *18*, 121–129. [CrossRef]
18. Senturk, E.; Adil, M.A.; Saqib, M. Ionospheric total electron content response to annular solar eclipse on June 21, 2020. *Adv. Space Res.* **2020**, *67*, 1937–1947. [CrossRef]
19. Sun, Y.Y.; Chen, C.H.; Su, X.; Wang, J.; Yu, T.; Xu, H.R.; Liu, J.Y. Occurrence of nighttime irregularities and their scale evolution in the ionosphere due to the solar eclipse over East Asia on 21 June 2020. *J. Geophys. Res. Space Phys.* **2023**, *128*, e2022JA030936. [CrossRef]
20. Richmond, A.D.; Fang, T.-W.; Maute, A. Electrodynamics of the equatorial evening ionosphere: 1. Importance of winds in different regions. *J. Geophys. Res. Space Phys.* **2015**, *120*, 2118–2132. [CrossRef]
21. Richmond, A.D.; Fang, T.W. Electrodynamics of the equatorial evening ionosphere: 2. Conductivity influences on convection, current, and electrodynamic energy flow. *J. Geophys. Res. Space Phys.* **2015**, *120*, 2133–2147. [CrossRef]
22. Fesen, C.G.; Crowley, G.; Roble, R.G.; Richmond, A.D.; Fejer, B.G. Simulation of the pre-reversal enhancement in the low latitude vertical ion drifts. *Geophys. Res. Lett.* **2000**, *27*, 1851–1854. [CrossRef]
23. Stoneback, R.A.; Heelis, R.A.; Burrell, A.G.; Coley, W.R.; Fejer, B.G.; Pacheco, E. Observations of quiet time vertical ion drift in the equatorial ionosphere during the solar minimum period of 2009. *J. Geophys. Res. Space Phys.* **2011**, *116*, A12327. [CrossRef]
24. Nanan, B.; Chen, C.Y.; Rajesh, P.K.; Liu, J.Y.; Bailey, G.J. Modeling and observations of the low latitude ionosphere-plasmasphere system at long deep solar minimum. *J. Geophys. Res.* **2012**, *117*, A08316. [CrossRef]
25. Tian, Z.; Sui, Y.; Zhu, S.; Sun, Y.-Y. Enhancement of electron density in the ionospheric F2 layer near the first contact of the total solar eclipse on 21 August 2017. *Earth Space Sci.* **2022**, *9*, e2021EA002016. [CrossRef]
26. Rishbeth, H. The F-layer dynamo, *Planet. Space Sci.* **1971**, *19*, 263–267. [CrossRef]
27. Farley, D.T.; Bonelli, E.; Fejer, B.G.; Larsen, M.F. The prereversal enhancement of the zonal electric field in the equatorial ionosphere. *J. Geophys. Res. Atmos.* **1986**, *91*, 13723–13728. [CrossRef]
28. Verhulst, T.G.W.; Stankov, S.M. Height dependency of solar eclipse effects: The ionospheric perspective. *J. Geophys. Res. Space Phys.* **2020**, *125*, e2020JA028088. [CrossRef]
29. Liu, L.; Chen, Y.; Le, H.; Ning, B.; Wan, W.; Liu, J.; Hu, L. A case study of postmidnight enhancement in F-layer electron density over Sanya of China. *J. Geophys. Res. Space Phys.* **2013**, *118*, 4640–4648. [CrossRef]
30. Liu, L.; Ding, Z.; Le, H.; Chen, Y.; Zhang, H.; Wu, J.; Li, G.; Wan, W. New features of the enhancements in electron density at low latitudes. *J. Geophys. Res. Space Phys.* **2020**, *125*, e2019JA027539. [CrossRef]

31. Brace, L.H.; Theis, R.F. An empirical model of the interrelationship of electron temperature and density in the daytime thermosphere at solar minimum. *Geophys. Res. Lett.* **1978**, *5*, 275–278. [CrossRef]
32. Oyama, K.I.; Watanabe, S.; Su, Y.; Takahashi, T.; Hirao, K. Season, local time, and longitude variations of electron temperature at the height of 600 km in the low latitude region. *Adv. Space Res.* **1996**, *18*, 269–278. [CrossRef]
33. Balan, N.; Oyama, K.I.; Bailey, G.J.; Fukao, S.; Watanabe, S.; Abdu, M.A. Electron temperatures in the F region of the ionosphere: Theory and observation. *Rev. Geophys.* **1978**, *16*, 355–399. [CrossRef]
34. Bilitza, D. Models for the relationship between electron density and temperature in the upper ionosphere. *J. Atmos. Terr. Phys.* **1975**, *37*, 1219–1222. [CrossRef]
35. Balan, N.; Oyama, K.I.; Bailey, G.J.; Fukao, S.; Watanabe, S.; Abdu, M.A. A plasma temperature anomaly in the equatorial topside ionosphere. *J. Geophys. Res. Space Phys.* **1997**, *102*, 7485–7492. [CrossRef]
36. Oyama, K.I.; Abdu, M.A.; Balan, N.; Bailey, G.J.; Watanabe, S.; Takahashi, T.; Paula, E.R.; Batista, I.S.; Isoda, F.; Oya, H. High electron temperature associated with the prereversal enhancement in the equatorial ionosphere. *J. Geophys. Res. Space Phys.* **1997**, *102*, 417–424. [CrossRef]